small method
www.small-methods.com

Large-Range HS-AFM Imaging of DNA Self-Assembly through In Situ Data-Driven Control

*Adrian P. Nievergelt, Christoph Kammer, Charlène Brillard, Eva Kurisinkal, Maartje M. C. Bastings, Alireza Karimi, and Georg E. Fantner**

Understanding hierarchical self-assembly of biological structures requires real-time measurement of the self-assembly process over a broad range of length- and timescales. The success of high-speed atomic force microscopy (HS-AFM) in imaging small-scale molecular interactions has fueled attempts to introduce this method as a routine technique for studying biological and artificial self-assembly processes. Current state-of-the-art HS-AFM scanners achieve their high imaging speed by trading achievable field of view for bandwidth. This limits their suitability when studying larger biological structures. In ambient conditions, large-range scanners with lower resonance frequencies offer a solution when combined with first principle model–based schemes. For imaging molecular self-assembly processes in fluid, however, such traditional control techniques are less suited. In liquid, the time-varying changes in the behavior of the complex system necessitate frequent update of the compensating controller. Recent developments in data-driven control theory offer a model-free, automatable approach to compensate the complex system behavior and its changes. Here, a data-driven control design method is presented to extend the imaging speed of a conventional AFM tube scanner by one order of magnitude. This enables the recording of the self-assembly process of DNA tripods into a hexagonal lattice at multiple length scales.

Macromolecular systems with the ability to dynamically assemble and disassemble are ubiquitous throughout technology and nature. Prominent examples are the dynamic self-assembly of microtubules[1] and actin filaments[2,3] in the cytoskeleton of mammalian cells, or networked chemical systems based on nanoparticles.[4] Often, such self-assembly systems exhibit both short-range ordering into a crystal and large-range effects such as grain boundary formation. In order to understand grain boundary formation and defect healing, one has to observe individual crystal constituents and their interactions close to the boundary. Therefore, a microscope with very high spatiotemporal resolution that is additionally capable of a large field of view is required. Atomic force microscopy (AFM), and in particular high-speed AFM (HS-AFM), has proven to be an invaluable tool to study a wide range of dynamic biological processes.[5–9] However, high-speed scanners generally only have a small displacement,[10,11] and even high-speed scanners designed specifically for a larger field of view are limited in range.[12,13] More traditional scanners such as piezo-tube-based designs offer scan ranges of 120 µm × 120 µm or more but suffer from low resonance frequencies that limit the scanning speed severely. When a voltage step is applied to a scanner, the scanner's mechanical resonances will be excited, leading to a characteristic ring-down behavior. The dynamics of a liquid meniscus add complex additional resonances to the primary ringing that are difficult to model (**Figure 1**a). When such dynamics are present in a traditional proportional–integral (PI) controller–based closed-loop system, as is the case with AFM, increasingly aggressive gains will first amplify the resonances of the system, and finally make the system entirely unstable (Figure 1b). Even if the system is still stable, the amplification of the scanner resonances results in ringing artifacts during imaging (Figure 1c, lower left) that obscure the real topography (Figure 1c, upper right). Previously, it has been shown that robust model–based control techniques can solve this problem.[14,15] Unfortunately, these techniques have not found widespread adoption, since the controller design process involved is extensive (Figure 1e) and error-prone, requiring the AFM user to have expert knowledge in control system engineering. Especially for experiments that need to be performed in solution, the complex system response, evaporation, and capillary motion of the liquid make the dynamic behavior of the scanner highly time-varying (Figure 1d), which makes it necessary to frequently redesign the controller. The difficulty in generating good models and the time-varying nature of the system make the implementation of model-based control design techniques impractical. In addition, the result needs to

Dr. A. P. Nievergelt, C. Brillard, Prof. G. E. Fantner
Laboratory for Bio- and Nano-Instrumentation
Ecole Polytechnique Fédérale de Lausanne (EPFL)
1015 Lausanne, Switzerland
E-mail: georg.fantner@epfl.ch
Dr. C. Kammer, Dr. A. Karimi
Automatic Control Laboratory
Ecole Polytechnique Fédérale de Lausanne (EPFL)
1015 Lausanne, Switzerland
E. Kurisinkal, Prof. M. M. C. Bastings
Programmable Biomaterials Laboratory
Ecole Polytechnique Fédérale de Lausanne (EPFL)
1015 Lausanne, Switzerland
The ORCID identification number(s) for the author(s) of this article can be found under https://doi.org/10.1002/smtd.201900031.

DOI: 10.1002/smtd.201900031

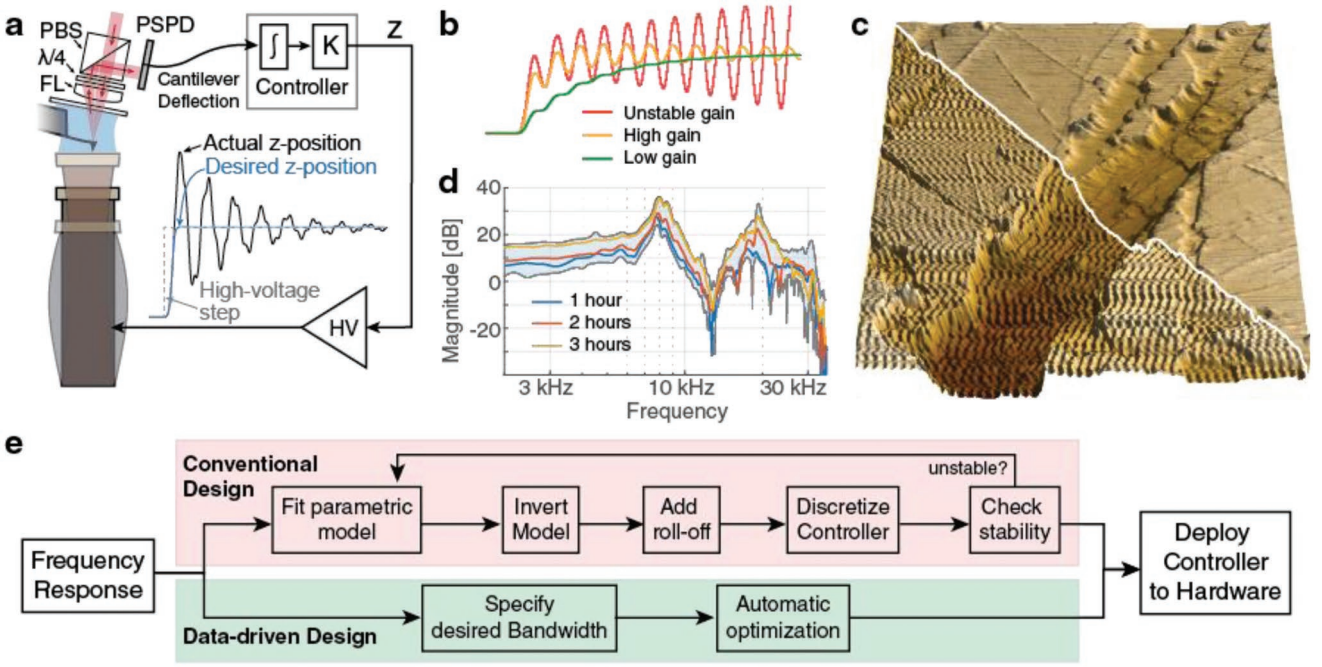

Figure 1. Structural resonances cause instability in AFM feedback, but can be compensated. a) Schematic of AFM control loop, consisting of the high-voltage amplifier, scanner, cantilever, readout optics, a position sensitive photodiode, and the controller, consisting of an integrator and a finite-order infinite-impulse response filter K. The scanner acts as a resonator and steps in position introduce complex ringing behavior. b) In closed-loop operation, the ringing of the scanner resonance is amplified by the feedback loop, which for increasingly aggressive gains first introduces visible ringing in the image (green and yellow trace, bottom triangles of height and error images) and finally leads to complete instability (red trace). c) Setting feedback gains too aggressively amplifies structural resonances that result in strong ripples in the measurement that follow the topography (lower triangle). When using less aggressive settings, the image resolves clearly without ringing (upper triangle). d) When operating in liquid, the dynamic response of the system is highly time-varying due to evaporation and movement of the liquid. Dynamic responses are recorded every 2 min. Representative examples are shown at different times into the experiment: 1 h (blue trace), 2 h (red trace), and 3 h (yellow trace). The envelope of all recorded traces is shaded as light blue in the background. e) Steps required for conventional model–based control requiring active user interaction, extensive knowledge in control system design, and significant time to execute. Using data-driven controller design, the process is simplified and the only user input required is the specification of a desired closed-loop feedback bandwidth.

be verified for stability to prevent deployment of an unstable controller. To avoid these issues, we propose to apply a novel control design method, data-driven robust (DaRt) control,[16,17] which is particularly well suited to controlling AFM scanners in liquid. The proposed method requires minimal user interaction, guarantees closed-loop stability,[16] and is fully automated (Figure 1e, green process), needing only a desired closed-loop bandwidth as input from the user. This automation enables the user to compute a controller and start the experiment within less than a minute. Our approach can compensate almost arbitrary resonances and is therefore suitable for a wide range of different scanners (see Figure S1 in the Supporting Information), and allows for fast scanning without compromising scan range. In our implementation, we use the cantilever directly as a sensor to measure the frequency response. This allows to achieve superior controller performance, since the measured response is not only that of the scanner, but that of the whole loop including discrete time delays, amplifier dynamics, scanner dynamics, and potentially cantilever dynamics.

In order to record high-resolution images such as DNA tripod self-assembly, sharp tips are necessary. A common concern in control design for AFM is tip wear or damage due to the identification process. In our implementation, we use a pseudorandom binary sequence (PRBS) as identification signal, which has an optimal crest factor of 1. In contrast to swept sine as used by a lock-in amplifier, the output signal observed on the cantilever deflection is only minimally perturbed away from its set point, indicating that the scanner is not extended significantly during identification. In addition, the nominal amplitudes we use for identification are between 0.5 and 5 nm. In our experiments, we have not observed damage to the tip or the substrate during identification. Thus, we conclude that the tip-sample forces from this type of identification are not large enough to cause damage to the tip. On the contrary, the better control over the feedback error during scanning reduces tip-sample forces during imaging and helps to preserve the tip.

Figure 2 shows an example of the typical performance that can be achieved with the proposed method. The dynamics of a commercial tube scanner (Bruker AS-12VLR, 12 µm range) operated in a liquid environment (Figure 2a, green trace) show a multitude of resonances. The designed controller (Figure 2a, red trace) is the result of the automated optimization with the objective of having the closed-loop response of the identified system to behave like a 20 kHz second-order Butterworth low-pass filter (see Section 2 in the Supporting Information for details on the formulation and optimization). This control design is based purely on the measured frequency response of the system, and does not require a parametric model.

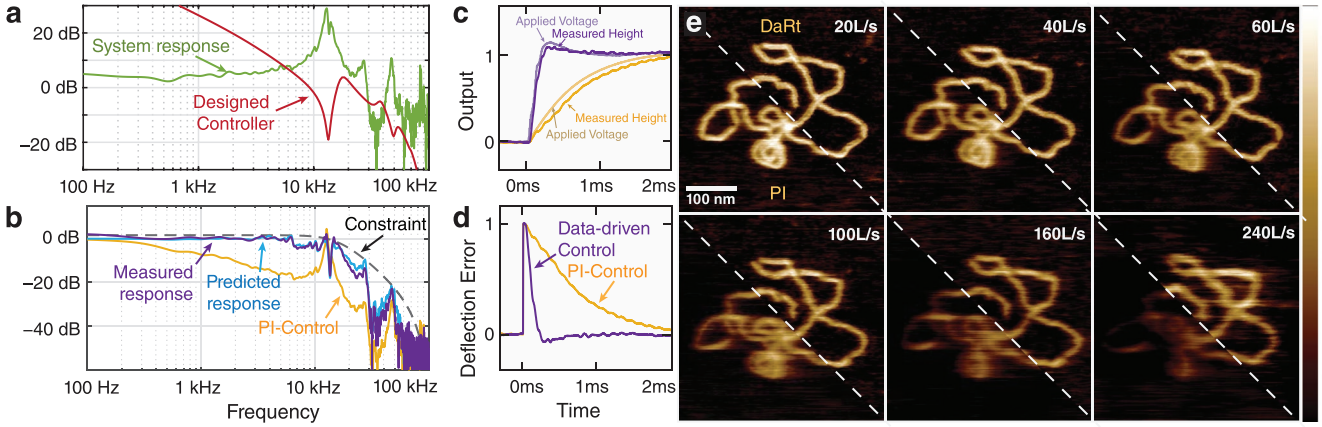

Figure 2. Performance of the proposed control system design method for high-speed scanning. a) Amplitude response spectra of the microscope in axial direction (green trace) and of the controller designed by DaRt control design (red trace). b) Predicted (blue trace) and measured closed-loop response of the microscope (purple trace) as well as measured response of a PI controller (yellow trace). In contrast to the PI controller, the applied voltage of the DaRt controller contains the complex compensation dynamics that are absent in the measured height by design. The closed-loop response of the data-driven controller is constrained to be below the frequency constraint (dashed black trace). The topography adjustment (c) in response to a deflection error step (d) is significantly faster when using DaRt control (purple traces) than when using traditional PI control (yellow traces). e) DNA plasmid scanned at increasing line rate in buffer solution. Without filtering (bottom left triangle), the DNA becomes blurred already at 40 lines s^{-1} and completely unrecognizable at 160 lines s^{-1}. In contrast, using a feedback with filters (upper right triangle) preserves the topography well up to high line rates. *z*-scale is 0–2.5 nm.

When implemented in the AFM (see Figures S2–S4 in the Supporting Information), the measured closed-loop response (Figure 2b, purple trace) is almost identical to the theoretical response that is predicted by the optimization routine (Figure 2b, blue trace). A step applied to the deflection signal visualizes the much improved positioning speed (Figure 2c) and recovery of the set point (Figure 2d) when using DaRt control compared to traditional PI control. To demonstrate the improved performance, we have imaged plasmid DNA in buffer solution (Figure 2e; see Section 7 in the Supporting Information for full images) at increasing scan rates. By using our previously developed high-speed head[18,19] in photothermal off-resonance tapping (PORT)[20] with commercially available high-speed cantilevers (Olympus BLAC-10DS), we ensure a high enough measurement bandwidth to capture all relevant dynamics of the system (200 kHz sampling rate, 195 lines s^{-1} limit for one measurement per pixel at 512 pixels). Even at a relatively low scan speed of 20 lines s^{-1}, the image taken with the new controller (top right triangle) appears sharper than with a pure PI controller (lower left triangle). When increasing the scan speed, using the PI controller quickly results in a blurred image, while DaRt control preserves sharp edges up to 100 lines s^{-1}. When increasing the speed further, the improved controller likewise starts blurring the DNA; however, the pure PI controller cannot track features at all anymore (≈1 order of magnitude better tracking at 10 kHz; see Figure S4a in the Supporting Information). Finally, DaRt control can not only be used for real-time compensation of resonance in the *z*-direction, but can also be applied to correcting lateral resonances (see Section 6 in the Supporting Information).

We utilized the capabilities of our new technique to resolve the self-assembly dynamics of hexagonal lattices formed using DNA nanotechnology. Planar tripods with blunt ends are formed from three distinct strands.[21] While the blunt ends weakly interact with each other,[22] the tripods do not form lattices in solution, even when annealed.[21] When weakly adsorbed to a surface, however, the reduction in degrees of freedom increases the effective dissociation constant and leads to the formation of nominally hexagonal 2D crystals. Together, these properties make the blunt-end assembly of DNA an excellent example of a highly dynamic, surface-enhanced process with short-range as well as long-range ordering. Using a conventional tube scanner and the DaRt controller, we can observe the formation of DNA patterns at multiple length scales (**Figure 3**a; full images in Figure S6 in the Supporting Information). We have acquired time-lapse recordings of nucleation and formation of hexagonal lattices (Figure 3b; Video S1, Supporting Information). While the 2D crystals form nominally hexagonal patterns, we observe a significant number of pentagonal and heptagonal structures, especially in the early stages of nucleation and growth. In our observations, these species are less stable than hexagons and growth seems to occur preferably in hexagonal patterns. In order to quantify defect density and location, we have used computer-vision-based segmentation and classification on the time-lapse dataset (details in the Experimental Section). Using the large range of our scanner, we can analyze the crystallization process over a wide range of different fields of view (Figure 3c). The result of the automated segmentation and classification is overlaid on the images (top right triangle). We find that a heptagonal defect is often accompanied by two pentagonal ones (Figure 3d). We hypothesize that this is necessary to minimize the lattice energy in the presence of defects. Figure 3e shows the surface density of all three polygonal species over time. Notably, the combined density of defects is initially larger than the density of hexagons. This is likely due to the high flexibility of the DNA tripods that makes pentagonal and heptagonal assemblies likely as long as there is no lattice to stabilize the hexagonal symmetry. Indeed, after the initial nucleation, the defect density seems to saturate while the growth of hexagonal patches is observed to continue at near

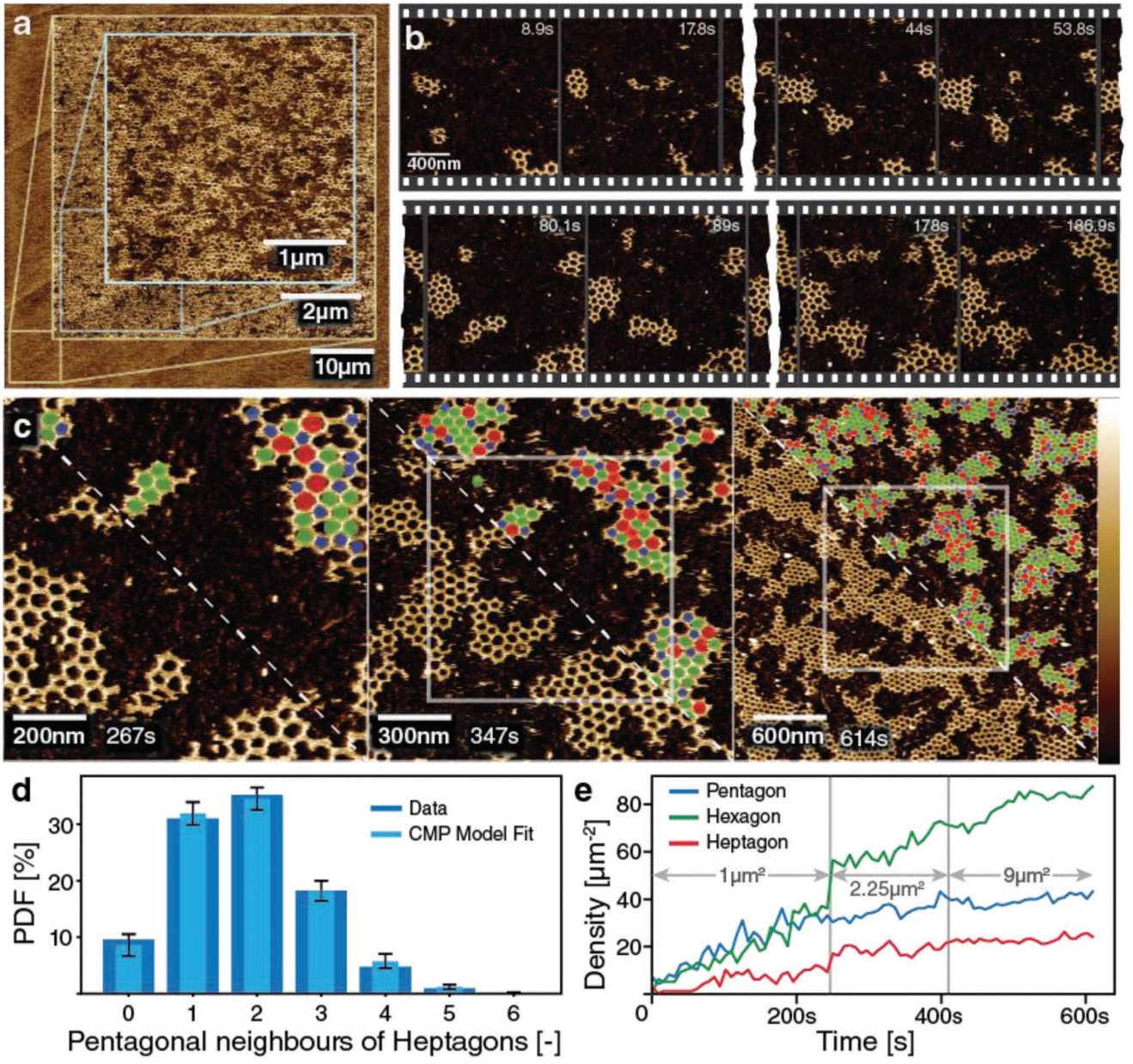

Figure 3. DNA tripod constructs assemble by blunt-end stacking on mica into a mostly hexagonal lattice with pentagonal and heptagonal defects. a) The scan area of interest can be directly observed and selected from 60 µm × 60 µm to 3 µm × 3 µm. b) Individual frame grabs of the early nucleation and growth of lattice patches scanned at 60 lines s^{-1}. *z*-scale is 0–3 nm. c) Consecutive increase of the field of view (last smaller indicated by white rectangle) during the assembly process shows large-scale patch formation. Lattice segmentation and classification into pentagons (blue), hexagons (green), and heptagons (red) is overlaid on the images (top right triangle). *z*-scale is 0–3 nm. d) Number statistic of pentagonal defects next to heptagonal defects, indicating preferred two pentagonal neighbors per heptagonal defect. The data (dark blue bars) fits well with a Conway–Maxwell–Poisson model (light blue bars, $\lambda = 3.71$, $\nu = 1.78$, error bars are 2σ model uncertainty). e) Surface densities of pentagons, hexagons, and heptagons in the recorded time lapse over different fields of view of the same process. Hexagonal lattice patches continue to grow while defect density saturates with a roughly 2:1 ratio of pentagons to heptagons.

constant rate. Notably, the steady-state density of pentagonal to heptagonal defects is close to 2:1, which has been suggested as the energetically lowest defect structure for graphene.[23]

The recording of the self-assembly of DNA tiles into a planar crystal on a variety of different size scales demonstrates the capabilities of our method to increase the scanning speed of most AFM scanners by an order of magnitude while fully preserving the lateral range of the scanner, even when measuring in liquid environment. Additionally, the process provides an optimal, but user-adjustable, *I*-gain that generally yields the best possible results for the system. This eliminates a difficulty that usually requires the skill of the microscope operator. Unless the feedback is limited by the dynamics of the cantilever, such as is the case for large and soft cantilevers, DaRt control

can be applied to virtually any commercial or custom-built AFM in any environment, either integrated into the existing controller or by bypassing the feedback. We have shown here that the data acquired are of high enough quality for automated segmentation and classification and therefore provide an excellent starting point for studying phenomena of forming 2D crystals, such as grain boundary formation, defect formation and healing, or lattice strain. Finally, the technique can enable the measurement of surface kinetics and surface diffusion of macromolecular self-assembly systems.

Experimental Section

AFM Imaging: Images have been acquired on a home-built small cantilever AFM with photothermal excitation as described elsewhere.[9,19,24] All images in the paper were acquired using PORT at frequencies between 120 kHz (DNA assembly) and 200 kHz (plasmid scanning) using AC10DS cantilevers (Olympus) with electron beam deposited carbon tips.[9]

A custom-made silicon O-ring was placed onto freshly cleaved mica and was half-filled by 5×10^{-3} M degassed $MgAc_2$ (diluted from 100×10^{-3} M filtered $MgAc_2$ solution with ultrapure water). The cantilever was approached to the surface and the surface was scanned to check for contaminations. After the identification and controller design process was performed, the cantilever was retracted from the surface by 1 µm and 10 µL of the DNA tripod solution was injected close to the cantilever in the dedicated channel of the cantilever holder. The sample was then scanned at a line rate of 60 Hz (1024 × 512 pixels), with *I*-gain set to the one provided by the controller design and the set point minimized while preserving good tracking.

AFM Image Processing: Time-lapse sequences were processed using an in-house developed batch processing extension to Gwyddion. Images were treated, in order, with a two-pixel conservative denoising filter, median line mismatch corrected, preflattened (Flatten Base operation), and finally polynomially line-by-line corrected with an Otsu's mask. Images were then exported in PNG format and assembled into a movie using FFMPEG.

Still images were manually flattened using a combination of plane flattening and masked line matching steps. Small scars were removed by masking where applicable for better visibility.

Segmentation and Classification of Time-Lapse Data: Exported grayscale images were loaded into a custom analysis script written in Python. Images were blurred with a nine-pixel Gaussian kernel (for 1 µm and 1.5 µm field of view) and thresholded with an Otsu method. The centers of lattice polygons have been found with the SimpleBlobDetector class from the OpenCV library. Image subsets were generated based on the center coordinates and typical lattice polygon size (side length ≈26 nm). Subsequently, classes for pentagonal, hexagonal, and heptagonal lattice elements were generated and asymmetry and rotation were determined by basin hopping optimization,[25] while the template offsets were matched by OpenCV template matching. Classification was then based on the highest match between the template and the image subset among the pentagonal, hexagonal, or heptagonal template.

Frequency Response Measurement: Acquisition of the frequency-domain system response was performed by bringing the AFM into feedback with the surface using either contact mode or PORT and then reducing the gains to small enough values to only compensate drift. The height output was modulated with a PRBS of order 10–12 with a nominal amplitude between 0.5 and 5 nm, depending on the noise level of the system and cantilever used. The deflection was synchronously recorded and frequency-domain spectra were calculated using the MATLAB *spa* function with a Hann window length of 700.

Control System Design: A novel data-driven method for robust control design based on convex optimization was employed.[16] A key feature was that only the frequency response of the plant was required for the design, and no parametric model was required. A fully parameterized fixed-structure transfer function controller of order 10[26] was designed directly in discrete time. This had the advantage that no controller discretization step was needed, and that the computed parameters can be directly written to the hardware. While a controller order of 10 had been sufficient for all of our systems, the order of the controller was user selectable and can be, limited by our implementation, increased up to 16 if a system with very complex dynamics were to be controlled for. In order to achieve a desired closed-loop bandwidth while guaranteeing robustness, the control performance was specified as a loop-shaping problem in the H_2 sense with additional H_∞ constraints. A detailed mathematical formulation as well as the implementation of the optimization is given in Section 2 in the Supporting Information.

Controller Implementation: The computed controller was deployed directly to the FPGA (PXIe-7975R with NI 5782 I/O-module) by the LabVIEW software module. The filters were implemented as eight serial second-order sections in transposed form II design, resulting in a maximum controller order of 16. This filter block was applied to the *z*-positioning output. Finally, the control loop was closed over the process variable with a digital integrator. While the algorithm computes an ideal integral gain to be used, the value can be optionally tuned by the operator. Each section can be individually disabled in real time to reduce computational delays in the feedback. A more exhaustive description of the controller implementation is given in Section 3 in the Supporting Information.

Plasmid DNA Preparation: pUC19 plasmid (X911.1) was bought from Carl Roth (Switzerland) in lyophilized condition and rehydrated with Buffer A (10×10^{-3} M 4-(2-hydroxyethyl)-1-piperazineethanesulfonic acid, pH 7.3) to a concentration of 25 µg mL^{-1}. To remove small DNA fragments, the sample was purified using analytical size exclusion chromatography in a Superose 6 10/300 column on an ÄKTA Pure system (GE Healthcare), resulting in a final concentration of 7 µg mL^{-1} for the main fraction.

The DNA sample for AFM was then prepared by pipetting 20 µL of 20×10^{-3} M $NiCl_2$ onto freshly cleaved mica, diluting this drop with 20 µL of Buffer A, and finally adding 4 µL of the purified DNA solution.[27] The sample was left to incubate for about 5 min before imaging.

DNA Tripod Preparation: ssDNA strands 1 (0.6×10^{-6} M), 2 (0.6×10^{-6} M), and 3 (1.8×10^{-6} M) were annealed in 5×10^{-3} M tris(hydroxymethyl)aminomethane (TRIS) (BioRad, Cat. No. 161-0716), 1×10^{-3} M ethylenediaminetetraacetic acid (EDTA) (abcr, Cat. No. 60-00-4), and 10×10^{-3} M $MgAc_2$ (abcr, Cat. No. 16674-78-5) buffer as previously reported.[21] The samples were annealed at 80 °C for 5 min, 60 °C for 10 min, cooled at a rate of 1 °C h^{-1} from 60 to 20 °C for 40 cycles, held at 20 °C for 10 min, and stored at 4 °C. Purification of the annealed product was conducted by running the sample on a 3% agarose gel and excising the band. The flow through was collected from Freeze 'N Squeeze gel extraction spin columns (Bio-Rad, Cat. No. 732-6165) according to manufacturer's instructions. The flow through was pipetted into VIVASPIN TURBO 4, MWCO 3000 (Sartorius, Ref. VS04T91) and centrifuged for 10 min at 4350 RCF. The retained solution containing the purified tripods was concentrated in a speed vacuum (IR Micro-Cenvac NB-503CIR) at 5000 rpm for 6 h at 35 °C. The concentration of the purified tripods was measured by UV–vis spectroscopy. The purified DNA tripods concentration was adjusted to 2.4×10^{-6} M in 5×10^{-3} M TRIS, 1×10^{-3} M EDTA, and 10×10^{-3} M $MgAc_2$ buffer prior to imaging.

ssDNA strand 1: 5′-ACTATGCAACCTGCCTGGCAAGCCTACGAT GGACACGGTAACG-3′

ssDNA strand 2: 5′-CGTTACCGTGTGGTTGCATAGT-3′

ssDNA strand 3: 5′-AGGCACCATCGTAGGTTT CTTGCCAGGCACCA TCGTAGGTTTCTTGCCAGGCACCA TCGTAGGTTTCTTGCC-3′

Supporting Information

Supporting Information is available from the Wiley Online Library or from the author.

Acknowledgements

The authors would like to thank Niccolò Banterle from UPGON at EPFL for help with DNA size exclusion chromatography. The authors would also like to acknowledge Moritz Durtschi for initial observations on blunt-end DNA tripods. This work was funded by the European Union's Seventh Framework Programme FP7/2007-2011 under grant agreement 286146, as well as the European Union's Seventh Framework Programme FP7/2007-2013/ERC grant agreement 307338.

Conflict of Interest

The authors declare no conflict of interest.

Keywords

control system design, DNA nanotechnology, high-speed atomic force microscopy, resonance compensation, self-assembly

Received: January 9, 2019
Revised: March 22, 2019
Published online: May 9, 2019

[1] E. M. Mandelkow, *J. Cell Biol.* **1991**, *114*, 977.
[2] T. Lehto, M. Miaczynska, M. Zerial, D. J. Müller, F. Severin, *FEBS Lett.* **2003**, *551*, 25.
[3] S. H. Lee, R. Dominguez, *Mol. Cells* **2010**, *29*, 311.
[4] B. A. Grzybowski, K. Fitzner, J. Paczesny, S. Granick, *Chem. Soc. Rev.* **2017**, *46*, 5647.
[5] T. Ando, N. Kodera, E. Takai, D. Maruyama, K. Saito, A. Toda, *Proc. Natl. Acad. Sci. USA* **2001**, *98*, 12468.
[6] N. Kodera, D. Yamamoto, R. Ishikawa, T. Ando, *Nature* **2010**, *468*, 72.
[7] J. Preiner, N. Kodera, J. Tang, A. Ebner, M. Brameshuber, D. Blaas, N. Gelbmann, H. J. Gruber, T. Ando, P. Hinterdorfer, *Nat. Commun.* **2014**, *5*, 4394.
[8] N. Chiaruttini, L. Redondo-Morata, A. Colom, F. Humbert, M. Lenz, S. Scheuring, A. Roux, *Cell* **2015**, *163*, 866.
[9] A. P. Nievergelt, N. Banterle, S. H. Andany, P. Gönczy, G. E. Fantner, *Nat. Nanotechnol.* **2018**, *13*, 696.
[10] N. Kodera, H. Yamashita, T. Ando, *Rev. Sci. Instrum.* **2005**, *76*, 053708.
[11] T. Fukuma, Y. Okazaki, N. Kodera, T. Uchihashi, T. Ando, *Appl. Phys. Lett.* **2008**, *92*, 243119.
[12] G. E. Fantner, G. Schitter, J. H. Kindt, T. Ivanov, K. Ivanova, R. Patel, N. Holten-Andersen, J. Adams, P. J. Thurner, I. W. Rangelow, P. K. Hansma, *Ultramicroscopy* **2006**, *106*, 881.
[13] H. Watanabe, T. Uchihashi, T. Kobashi, M. Shibata, J. Nishiyama, R. Yasuda, T. Ando, *Rev. Sci. Instrum.* **2013**, *84*, 053702.
[14] G. Schitter, P. Menold, H. F. Knapp, F. Allgöwer, A. Stemmer, F. Allgower, A. Stemmer, *Rev. Sci. Instrum.* **2001**, *72*, 3320.
[15] G. Schitter, R. W. Stark, A. Stemmer, *Ultramicroscopy* **2004**, *100*, 253.
[16] A. Karimi, C. Kammer, *Automatica* **2017**, *85*, 227.
[17] C. Kammer, A. P. Nievergelt, G. E. Fantner, A. Karimi, in *Proc. 20th Int. Fed. Autom. Control World Congr.*, Elsevier, Amsterdam, NL **2017**, pp. 10437–10442.
[18] J. D. Adams, A. Nievergelt, B. W. Erickson, C. Yang, M. Dukic, G. E. Fantner, *Rev. Sci. Instrum.* **2014**, *85*, 093702.
[19] A. P. Nievergelt, J. D. Adams, P. D. Odermatt, G. E. Fantner, *Beilstein J. Nanotechnol.* **2014**, *5*, 2459.
[20] A. P. Nievergelt, C. Brillard, H. A. Eskandarian, J. D. McKinney, G. E. Fantner, *Int. J. Mol. Sci.* **2018**, *19*, 2984.
[21] Y. He, Y. Chen, H. Liu, A. E. Ribbe, C. Mao, *J. Am. Chem. Soc.* **2005**, *127*, 12202.
[22] C. Maffeo, B. Luan, A. Aksimentiev, *Nucleic Acids Res.* **2012**, *40*, 3812.
[23] I. Zsoldos, *Nanotechnol., Sci. Appl.* **2010**, *3*, 101.
[24] A. P. Nievergelt, S. H. Andany, J. D. Adams, M. T. Hannebelle, G. E. Fantner, in *IEEE Int. Conf. Adv. Intell. Mechatronics*, IEEE, Piscataway, NJ **2017**, pp. 731–736.
[25] D. J. Wales, J. P. K. Doye, *J. Phys. Chem. A* **1997**, *101*, 5111.
[26] K. Zhou, J. Doyle, K. Glover, *Robust and Optimal Control*, Prentice-Hall, Englewood Cliffs, NJ **1996**.
[27] A. Pyne, R. Thompson, C. Leung, D. Roy, B. W. Hoogenboom, *Small* **2014**, *10*, 3257.

